

Some like it Triaxial: the universality of Dark Matter Halo shapes and their evolution along the cosmic time

Giulia Despali^{1*}, Carlo Giocoli^{2,3,4}, Giuseppe Tormen¹

¹ *Dipartimento di Fisica e Astronomia, Università degli Studi di Padova, vicolo dell'Osservatorio 3, 35122, Padova, Italy*

² *Dipartimento di Fisica e Astronomia, Alma Mater Studiorum Università di Bologna, viale Berti Pichat, 6/2, 40127 Bologna, Italy*

³ *INAF - Osservatorio Astronomico di Bologna, via Ranzani 1, 40127, Bologna, Italy*

⁴ *INFN - Sezione di Bologna, viale Berti Pichat 6/2, 40127, Bologna, Italy*

ABSTRACT

We present a detailed analysis of dark matter halo shapes, studying how the distributions of ellipticity, prolateness and axial ratios evolve as a function of time and mass. With this purpose in mind, we analysed the results of three cosmological simulations, running an ellipsoidal halo finder to measure triaxial halo shapes. The simulations have different scales, mass limits and cosmological parameters, which allows us to ensure a good resolution and statistics in a wide mass range, and to investigate the dependence of halo properties on the cosmological model.

We confirm the tendency of haloes to be prolate at all times, even if they become more triaxial going to higher redshifts. Regarding the dependence on mass, more massive haloes are also less spherical at all redshifts, since they are the most recent forming systems and so still retain memory of their original shape at the moment of collapse. We then propose a rescaling of the shape-mass relations, using the variable $\nu = \delta_c/\sigma$ to represent the mass, which absorbs the dependence on both cosmology and time, allowing to find universal relations between halo masses and shape parameters (ellipticity, prolateness and the axial ratios) which hold at any redshift. This may be very useful to determine prior distributions of halo shapes for observational studies.

Key words: galaxies: halos - cosmology: theory - dark matter - methods: numerical

1 INTRODUCTION

Nowadays different observational campaigns agree on the standard cosmological model to explain and describe the structure formation in our Universe (Fu et al. 2008; Planck Collaboration et al. 2013a). In this scenario, almost 95% of the energy content on the Universe is in unknown forms of energy and matter, generally called dark energy and dark matter. The structure formation process occurs around the initial density peaks (Bardeen et al. 1986; Bond & Myers 1996; Ludlow & Porciani 2011; Paranjape & Sheth 2012; Paranjape et al. 2013) and proceeds hierarchically along the cosmic time: small systems collapse first, at high redshift, and then merge together forming more massive ones (Lacey & Cole 1993, 1994; Tormen 1998). Galaxy clusters are the largest virialized systems in the Universe and so the last to form: almost 80% of their mass is attributed to dark matter, while the rest to baryons, divided in *hot* (diffuse gas, 75%), *cold* (stars, 7%) and other forms (18%) (Ettori et al. 2009). They collapse as consequence of gravitational instability and grow as a result of different violent merging events (Tor-

men et al. 2004); many observations have captured them as characterised by multiple mass components (Postman et al. 2012; Zitrin et al. 2013a), elongated in the plane of the sky (Zitrin et al. 2013b) or along the line-of-sight (Morandi et al. 2011). Galaxy clusters are also characterised by the presence of many substructures, which are the cores of progenitor haloes accreted during the formation history and may contain galaxy cluster members (Giocoli et al. 2010a). The mass density distribution of relaxed haloes typically follows a well defined profile (Navarro et al. 1996) that has a logarithmic slope of -1 in the inner part and -3 toward the outskirts. The distance from the center at which the logarithmic slope approaches -2 defines the scale radius r_s from which we can define the concentration $c = R_{vir}/r_s$, where R_{vir} represents the virialisation radius of the system. Galaxy clusters can be used as cosmological probes since they are expected to follow a well defined concentration-mass relation (Neto et al. 2007; Zhao et al. 2009; Prada et al. 2011; Giocoli et al. 2012b) and their predicted abundance as a function of redshift is well portrayed (Sheth & Tormen 1999; Jenkins et al. 2001; Tinker et al. 2008). These may then be combined with other analyses for example cosmic shear (Schrabback et al. 2007, 2010), CMB primordial density fluctuation (Planck Collab-

* E-mail: giulia.despali@studenti.unpd.it

oration et al. 2013a), Sunyaev Zel'dovich effect and X-ray data (Roncarelli et al. 2007, 2010), two (Marulli et al. 2012, 2013) and three point correlation functions (Moresco et al. 2013).

However, the use of galaxy clusters as cosmological probes depends on how well structural properties – mass, concentration, triaxiality and subhalo abundance – can be recovered combining different observations. Many studies have revealed that the possibility to correctly estimate the mass and the concentration of the clusters is an open problem for X-ray, SZ and also optical observations. For example, different lensing analyses on numerical and pseudo-analytical clusters have shown that the estimated mass is on average biased to be lower than the true one (Becker & Kravtsov 2011; Meneghetti et al. 2010b). This is due to the fact that the dark matter haloes in which the clusters are embedded are typically prolate (Giocoli et al. 2012c), while most of the works still uses spherical models: we have a large probability to see them elongated in the plane of the sky and this leads to underestimate the mass if we limit ourselves to spherical halo boundaries which will not capture the whole halo. On the other hand, when the major axis of the halo ellipsoid is elongated along the line-of-sight we tend to overestimate the mass. A correct modeling of the halo triaxiality is therefore important in order to reach a better understanding of these biases and how structural properties can be recovered from the observations. The triaxiality of the halo is also responsible for the amplification of the Einstein radius size (both when the cluster is very elongated in the plane of the sky and along the line-of-sight) and of the generation a possible bias in the estimated concentration and in the measurement of the inner slope of the density profile (Giocoli et al. 2013). SZ and X-ray mass reconstructions tend to rely on the assumption that the systems are spherically symmetric and the hot gas is in hydrostatic equilibrium. Rasia et al. (2012) have shown that the X-ray mass are on average biased low by a large amount, highlighting both the presence of non-thermal pressure and temperature anisotropy in the inter cluster medium. In this context it is worth to notice that the discrepancy between X-ray, SZ and lensing mass appear not only when the cluster is not relaxed but also when its mass density distribution deviate from spherical symmetry. Combined multi-wavelength observations are thus important not only to understand the physical state of cosmic structures but also their shape.

The interpretation of observations requires a comparison with the predictions coming from theory and simulations (Limousin et al. 2013). For this reason, it is becoming more and more important to model the results of simulations with as much detail as possible, even if this is computationally more expensive. Dark matter haloes are usually identified in simulations as spherical systems, since it is quite easy, computationally speaking, and it is also proven to be a good approximation when calculating the main properties of the halo population, such as the mass function, the concentration and so on. Moreover, even if their boundaries are spherical, obviously matter inside them is not isotropically distributed and so even from a spherical distribution it is possible to compute the axial ratios and other shape parameters. Nevertheless, it is clear that considering all systems as spheres is a bit rough and so many works claim the need of a more realistic model, such as triaxial ellipsoids (Warren

et al. 1992; Jing & Suto 2002; Allgood et al. 2006; Despali et al. 2013). Being more precise and allowing a greater variety of shapes, this method is particularly useful when one wants to study dark matter halo shapes and determine their influence on observable 2D projected quantities.

A precise knowledge of the ellipticity and of the axial ratio distributions of galaxy cluster-size halos is fundamental also when observations from different bands are combined to recover the cluster mass (Morandi et al. 2010, 2012). In this case the distribution priors can be used to constrain both the ellipticity on the plane of the sky and the elongation along the line-of-sight of the cluster ellipsoid (Sereno et al. 2013).

Thus, the aim of this work is to study the shape of triaxial haloes and model its distribution, its evolution with redshift and the dependence on cosmology. In particular, we will analyse the distribution of the shape parameters (axial ratios, ellipticity and prolateness) as a function of halo mass and redshift; we will then present some universal relations and fitting formulae which may be used to retrieve the typical shape distribution at a certain time or for a certain mass bin, when a comparison with observations or a prediction is needed.

The structure of this paper is as follows. In Section 2 we present the numerical simulations used in this work and the post processing pipeline. Section 3 describes the results on shape parameters: we analyse the properties of the halo population at various redshifts of the simulations and show some universal fitting formulae for the shape parameters. In Section 4 we describe the merger tree catalogues and how it is possible to relate the shape with the formation redshift of haloes. Finally in Section 5 we summarise and discuss our results.

2 THE NUMERICAL SIMULATIONS

In this work we use the results of three different cosmological simulations. First, the GIF2 Simulation (Gao et al. 2004): it adopts a Λ CDM cosmological model with $\Omega_m = 0.3$, $\Omega_\Lambda = 0.7$, $\sigma_8 = 0.9$ and $h = 0.7$ and follows 400^3 particles in a periodic cube of side $110h^{-1}$ Mpc from an initial redshift $z = 49$ to the present time. The individual particle mass is $1.73 \times 10^9 h^{-1} M_\odot$. Initial conditions were produced by imposing perturbations on an initially uniform state represented by a glass distribution of particles (White 1996). Based on the Zel'dovich approximation (Zel'Dovich 1970), a Gaussian random field is set up by perturbing the positions of the particles and assigning them velocities according to the growing model solution of linear theory (Seljak & Zal-darriaga 1996).

Then, within a serie of new cosmological simulations, we ran Baby and Flora, using the publicly available code GADGET-2 (Springel 2005). In particular, Baby follows 512^3 particles in a periodic box of $100h^{-1}$ Mpc from $z = 99$ to the present time. The particle mass is $6.36 \times 10^8 h^{-1} M_\odot$ and adopts $\Omega_m = 0.307$ ($\Omega_b = 0.0483$ used to compute the transfer function), $\Omega_\Lambda = 0.693$, $\sigma_8 = 0.829$ and $h = 0.677$, following the recent Planck results (Planck Collaboration et al. 2013b). The initial power spectrum was generated with the code CAMB (Lewis et al. 2000) and initial conditions were produced perturbing a glass distribution with N-GenIC

	Ω_m	Ω_Λ	$H[\text{km s}^{-1}]$	box [$\text{Mpc } h^{-1}$]	z_i	N	$m_p[M_\odot h^{-1}]$	soft [$\text{kpc } h^{-1}$]	σ_8	$M_*(0)[10^{12}M_\odot h^{-1}]$
GIF2	0.3	0.7	70	110	49	400 ³	1.73×10^9	6.6	0.9	8.9
Baby	0.307	0.693	67.7	100	99	512 ³	6.36×10^8	5	0.829	4.9
Flora	0.307	0.693	67.7	2000	99	1024 ³	6.35×10^{11}	48	0.829	4.9

Table 1. Main features of the three simulations used in this work.

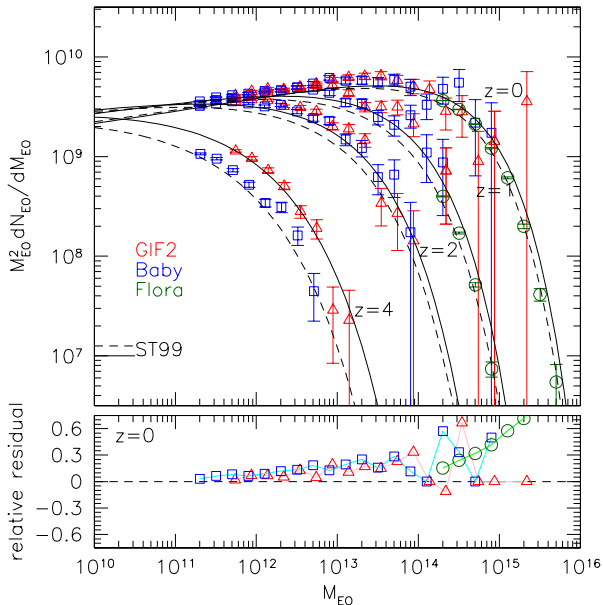


Figure 1. Halo mass function of the three simulations at four different z , obtained with the EO halo finder. Different data points and colors show the results for the three different simulations, and the error bars represent the Poisson uncertainty. The solid and dashed curves represent, respectively, the theoretical prediction for the GIF2 and Planck cosmology given by Sheth & Tormen (1999) mass function (ST99). The lower panel show the relative residuals between the halo abundance obtained with the EO and the SO finder for the three simulations at $z = 0$.

(<http://www.mpa-garching.mpg.de/gadget>). Flora follows 1024^3 particles in a periodic box of $2h^{-1}$ Gpc from $z = 99$, with the same cosmological model of the previous one. The particle mass is $6.35 \times 10^{11} h^{-1} M_\odot$ and has been run mainly to have a larger statistic for massive clusters-size haloes.

The combined use of two different cosmological models will allow us to shed more light on the possible dependence of the evolution of halo shape and evolution as a function of cosmological parameters. In Table 1 we summarize the parameters with which the three simulations have been run. For example, we see how the difference in cosmology produces a difference in M_* - the typical mass of haloes forming at the present time, which is identified by $\nu = \nu(z) = \delta_c(z)/\sigma(M) = 1$, where $\sigma^2(M)$ represents the variance in the initial density fluctuation field when smoothed on scale $R = (3M/4\pi\bar{\rho})^{1/3}$ and $\delta_c(z)$ is the linear overdensity threshold for collapse extrapolated at redshift z . At $z = 0$ for the GIF2 simulation $M_* = 8.9 \times 10^{12} M_\odot h^{-1}$, while for Baby $M_* = 4.9 \times 10^{12} M_\odot h^{-1}$ due to the different cosmological model.

2.1 Post-processing pipeline

At each simulation snapshot we first identified dark matter haloes as peaks in the density field adopting a Spherical Overdensity (hereafter SO) algorithm: we estimated the local dark matter density at the position of each particle by calculating the distance to the tenth closest neighbour and we assigned to each particle a local density $\rho \propto d_{10th}^{-3}$. Sorting particles in density, we choose as centre of the first halo the position of the densest particle. We then grow a sphere of matter around this centre and stop when the density within the sphere falls below the virial value appropriate for the cosmological model at that redshift; for the definition of virial density we adopted the model of Eke et al. (1996). Properties of all systems with more than 10 particles are stored by our halo finder (Tormen et al. 2004; Giocoli et al. 2008). In this way, for the three simulations, we obtain a catalogue of spherical virialized haloes for each snapshot.

Even if the SO algorithm has been proven to work very well in identifying haloes and it has also been shown that spherical haloes can be used to estimate the halo mass function and other properties quite precisely, it is also true that it is more realistic to describe haloes as triaxial ellipsoids, as within the context of the Ellipsoidal Collapse (hereafter EC) model (White & Silk (1979), Bond & Myers (1996), Sheth et al. (2001)). This is motivated by the fact that haloes are not isolated systems and that the surrounding gravitational field influences them during their collapse and formation phases; moreover during their hierarchical growth they experience different merging. All these effects stretch and modify the halo shape.

Thus, an ellipsoidal halo finder is particularly useful when one wants to study halo shapes, which are obviously more sensible than any other properties to the way in which haloes are identified. For this reason, after the SO algorithm we ran the Ellipsoidal Overdensity (hereafter EO) code described in Despali et al. (2013): it re-identifies all haloes previously found by the SO algorithm using an iterative method to obtain the best fitting ellipsoid to the particle distribution; still, halo boundaries are chosen using the virial overdensity. Note that, in principle, the EO algorithm could run on any pre-existing halo catalogue: we chose to use a combination of SO+EO algorithms to be more consistent, since both methods define haloes using a particular shape and since we need to grow a sphere as a first step of the EO (for the starting guess on the shape). We then calculated the mass tensor $M_{\alpha\beta}$ defined by the N particles found inside the ellipsoid as:

$$M_{\alpha\beta} = \frac{1}{N} \sum_{i=1}^N r_{i,\alpha} r_{i,\beta} \quad (1)$$

where \mathbf{r}_i is the position vector of the i th particle and α and β are the tensor indices. By diagonalizing $M_{\alpha\beta}$ we then ob-

tained the eigenvalues ($l_1 \geq l_2 \geq l_3$) and eigenvectors which define the shape and orientation of the virialized structure: the axes ($\lambda_1 \geq \lambda_2 \geq \lambda_3$) of the best fitting ellipsoid are defined as the square roots of the mass tensor eigenvalues: $\lambda_i = \sqrt{l_i}$. In this way we obtained another set of EO catalogues, equivalent to the SO one: we chose to keep only haloes formed by more than 200 particles to ensure a good resolution in the determination of the axes. The resulting ellipsoidal masses are slightly higher than the spherical ones (consistently to the fact that ellipsoids are expected to fit the actual density distribution better than spheres) and the resulting shapes are obviously more elongated (Despali et al. 2013). In Figure 1 we show the resulting ellipsoidal halo mass function at four different z for the three simulations; in particular for Flora we show only two redshifts since there are not many haloes resolved with more than 200 particles at redshift larger than one; the error bars represent the Poisson uncertainty. Solid and dashed line represent the halo mass function prediction by Sheth & Tormen (1999) for the two cosmologies of the simulations. In the lower panel, we show the relative residual between the mass functions obtained with the EO and SO finders at $z = 0$ (the behaviour at the other redshift is consistent with this one). Since the ellipsoidal and the spherical masses are positively biased with respect to each other of some percents, this results in a bias in the halo abundance that can reach 10–30% and that increases with halo mass due to the fact that massive haloes are intrinsically more elongated and so their mass and shape are captured much better by an ellipsoidal shape.

2.2 Halo shape parameters

As explained in the previous section, the axes of the best fitting ellipsoid for each halo are defined by the square roots of the mass tensor eigenvalues. The other relevant quantities that can be derived from the eigenvalues are the ellipticity e and prolateness p of each halo, that can be written as:

$$e = \frac{\lambda_1 - \lambda_3}{2\tau} \quad , \quad p = \frac{\lambda_1 - 2\lambda_2 + \lambda_3}{2\tau} \quad (2)$$

where $\lambda_{1,2,3}$ are the axes derived from the mass tensor eigenvalues and $\tau = \lambda_1 + \lambda_2 + \lambda_3$. Using this definitions, e quantifies the deviations from sphericity and p measures prolateness versus oblateness: by construction a sphere has $e = p = 0$. The fact that $\lambda_1 \geq \lambda_2 \geq \lambda_3 \geq 0$ introduces the boundaries $-e \leq p \leq e$, $p \geq 3e - 1$. This makes the points of the $e - p$ distribution populate only a triangle, as already shown in Bardeen et al. (1986), Porciani et al. (2002) and Desjacques (2008), and here in Figure 8 which we will discuss later on in the paper.

3 RESULTS: HALO POPULATIONS AT DIFFERENT Z

In this section we will describe how the halo ellipticity and prolateness change as a function of redshifts for different halo masses and how it is possible to obtain universal relations for the shape parameters.

3.1 Distributions of e and p at different times

In Figure 2 we show the ellipticity and the prolateness cumulative distributions: in each panel we present the results for five different redshifts - $z = 2, 1.5, 1, .5, 0$ - (or less at high masses) for a given mass bin. The haloes of Baby and Flora are represented together - since they have the same cosmology - by the solid lines, while those of the GIF2 by the dotted lines. Flora is determinant to have enough data at $M > 10^{14} M_\odot h^{-1}$: it contains around 150000 systems more massive than 10^{14} and 1390 still more massive than $10^{15} M_\odot h^{-1}$. Looking at each panel it is clear how both ellipticity and prolateness peak at higher values at high redshift; on the other hand, comparing the curves of the same colour in the four panels, we see that, at any given redshift, the median of e and p increases with mass: as already shown in other works using the axial ratios (Allgood et al. 2006; Muñoz-Cuartas et al. 2011), at the present time - and also at each previous epoch - the most massive systems are also the least spherical. They are still in the formation phase and so their shape is still be influenced by the direction of the last major merger or of the material falling in through the filaments, making them more elongated. Smaller haloes, formed at higher redshifts and typically more concentrated, lived for enough time to relax and lose memory of the directions of the different merging events experienced during their history. To stress these two dependencies, in Figure 3, we show, as a function of z - only for Baby+Flora - the medians of the ellipticity and of the prolateness distributions of Figure 2: each set of point shows the median relation for a different mass bin and the shaded regions the quartiles; the dashed lines represent the linear fit to each set of points.

In Figure 2, we observe also a slight dependence on cosmology, with Baby and Flora having an higher average value for both e and p ; this was expected since, in a universe with a lower value of σ_8 (Baby+Flora), haloes tend to form later and so, when we look at them at a given time, they are still more ellipsoidal than those which form with in an higher- σ_8 -universe (GIF2).

3.2 A universal rescaling for halo shape evolution

In Figure 4 we show how the ellipticity and prolateness distributions evolve in time for haloes of different masses: in the top panel the median ellipticity is plotted against the halo mass for eleven snapshots of each simulation (a part from Flora, we have a significant number of haloes only at six snapshots). We can notice both a dependence on mass and on time as in Figure 2: first, looking at each set of points independently, it is clear that more massive haloes are on average less spherical than the smaller ones. Then, looking at the whole plot, the median ellipticity decreases in time, leading to a more spherical distribution at the present time. In the bottom panel, we show the same results for prolateness. At all times haloes tend to be prolate ($p > 0$), even if this trend weakens at low redshifts.

Since the virial mass is a cosmology and redshift-dependent definition, Press and Schechter (PS) and extended-PS approaches (Press & Schechter 1974; Bond et al. 1991; Lacey & Cole 1993) have shown that an universal generalisation of the mass function can be obtained by using the variable $\nu(z)$. An analogous approach has also

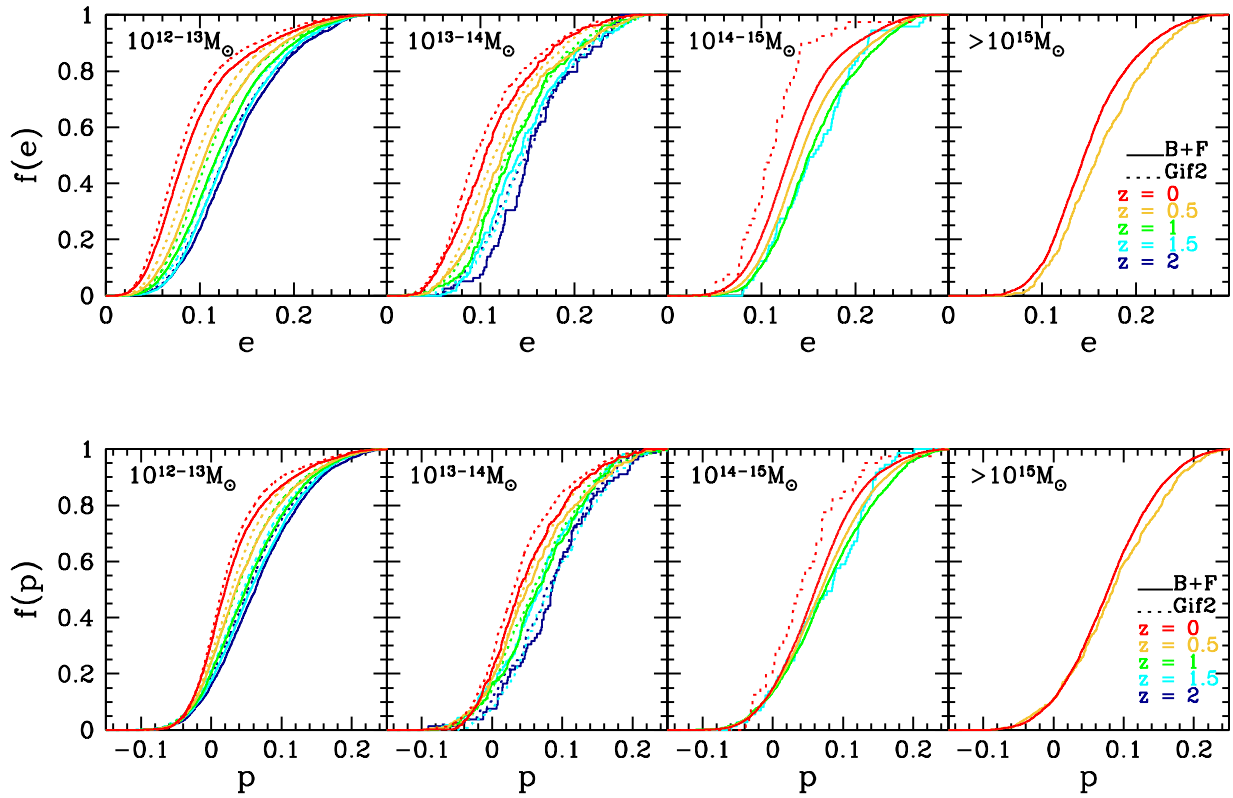


Figure 2. Ellipticity and prolateness cumulative distributions. Each panel shows the distribution at five redshifts for a different mass bin, with increasing mass from left to right. The haloes of Baby and Flora are represented by the solid lines, while those of the GIF2 by the dotted lines. We notice that both ellipticity and prolateness decrease to low redshift and also to lower masses.

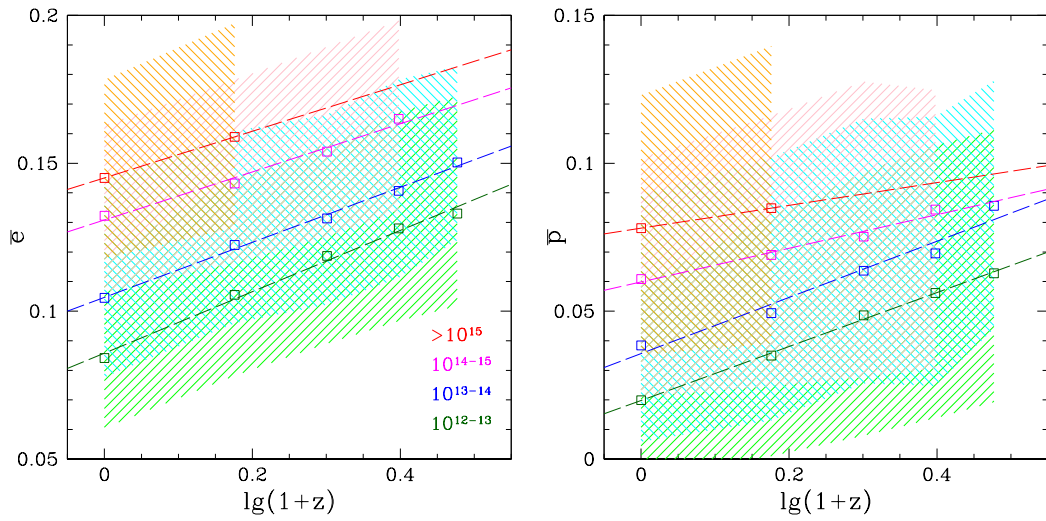


Figure 3. Medians and quartiles of the cumulative distributions of Figure 2 both for the ellipticity (left panel) and the prolateness (right panel), for Baby and Flora as a function of redshift. Each set of point shows the median relation for a different mass bin and the shaded regions the quartiles. The dashed lines represent the linear fit to each set of points.

been used by Prada et al. (2011) to rescale the concentration for different cosmologies and various redshifts. Also in our case, using ν instead of the virial mass, allows to obtain an universal relation: in Figure 5 we show the same points of Figure 4, but as a function of ν instead of mass. It is easy to see that the use on ν remove the dependence on both cosmology and time: this is due to the fact that $\sigma(M)$ retains the information of the mass and is higher for low masses, while $\delta_c(z)$ changes in time, increasing at high z . The combination of the three simulations allows us to span an order of magnitude in ν and we verify that, in these unit, all the points move on the same median relation. The effect is the same also on the prolateness and the axial ratios and so we believe that it is not worth showing all of them. Thus, in Figure 6 we decided to average over all the points at all the eleven redshifts, for each one of the simulations: the coloured points show the medians for each simulation and the corresponding shaded regions enclose the first and third quartile of each distribution. The black dashed line represents the best fit to all the points, which can be written as:

$$\begin{aligned} e &= 0.098_{-0.001}^{+0.001} \lg(\nu) + 0.0940_{-0.0001}^{+0.0002} \\ p &= 0.079_{-0.003}^{+0.003} \lg(\nu) + 0.025_{-0.001}^{+0.001}. \end{aligned} \quad (3)$$

The parameters and the errors were obtaining by fitting the distributions in both directions and then taking the mean values. For e , the interquartile difference goes from 0.05 at low values of ν to 0.08 at high ν ; for p it changes from 0.05 to 0.1. This reflects the fact that haloes at different redshifts populate different regions due to their relative mass limits, but they remain around it.

In Figure 7 we show the same results for the axial ratios (λ_3/λ_1 and λ_2/λ_1), which can be more useful for the comparison with observations. Looking at the axial ratios we recognise the same trends in the evolution of shapes that we noticed studying e and p . The best fit relations to all the data points are:

$$\begin{aligned} \frac{\lambda_3}{\lambda_1} &= -0.282_{-0.004}^{+0.003} \lg(\nu) + 0.567_{-0.001}^{+0.001} \\ \frac{\lambda_2}{\lambda_1} &= -0.293_{-0.005}^{+0.007} \lg(\nu) + 0.736_{-0.002}^{+0.002}. \end{aligned} \quad (4)$$

In this case the interquartile difference for λ_3/λ_1 goes from 0.17 at low ν to 0.19 at high ones; for λ_2/λ_1 it changes more, from 0.17 to 0.25.

3.3 e - p relation

As discussed in Bardeen et al. (1986), Porciani et al. (2002) and Desjacques (2008), the definition of e and p , together with the range of the eigenvalues, introduces a correlation between them at high ellipticities (which in particular it has been studied at the initial conditions). In what follows, we present the same distribution but using the catalogues of virialized haloes at each z . The ellipticity and prolateness of haloes still form a triangular region in the $e - p$ plane and it is interesting that the median distribution almost does not change with time (Figure 8): at high redshift, due to the limited mass resolution of the simulation, we have few haloes in our mass range, but nevertheless they already form a triangle; moving to lower redshift we have more and more haloes, which keep populating the triangle, but leave the median relation almost unchanged. The data points in

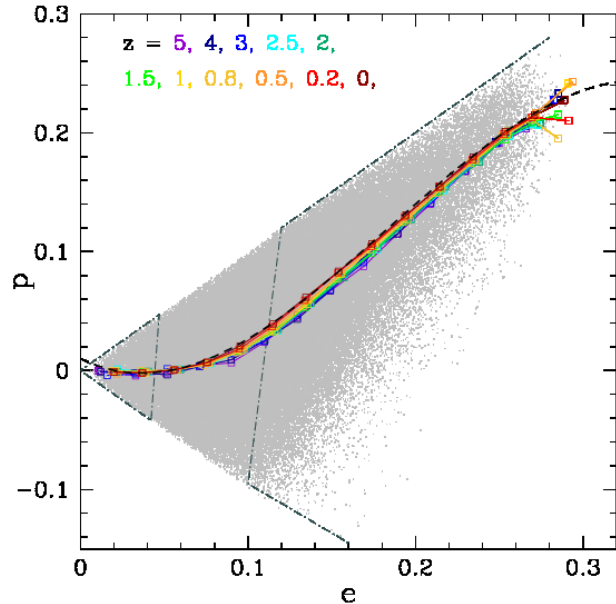


Figure 8. e - p distribution at eleven different redshifts, the same of Figure 4: the coloured points show the medians at a certain redshift taken on all the data of the three simulations together. The black dashed curve shows the fitting function to the points at $z = 0$. The gray dots represent the $e - p$ distribution at $z = 0$ for all the simulations; the dotted lines delimit the regions for which the relative difference between λ_1 and λ_3 is less than 25% (in the triangle on the left) or more than 50% (in the region on the right).

Figure 8 show the median distributions at eleven different redshifts, represented by the different color points. The small gray dots show the whole distribution at $z = 0$, for all the three simulations together. The points at $z = 0$ are fitted by the relation:

$$p = 0.01 - 0.7e + 10.57e^2 - 19.1e^3. \quad (5)$$

which is represented by the black dashed line; to fit the relation at the other snapshots it is enough to introduce a the dependence on redshift of the order of $(1+z)^{-0.05}$. The flat initial part, up to the fourth median point, corresponds to haloes for which both relative differences between the axes ($(\lambda_1 - \lambda_3/\lambda_1)$ and $(\lambda_1 - \lambda_2/\lambda_1)$) are less than 25%, while the linear growth at $e \geq 0.1$ is represented by haloes with $(\lambda_1 - \lambda_3/\lambda_1)$ greater than 50%. These two regions are marked in the figure by the dotted lines. This also confirms the tendency to prolateness already shown in other works: on average, the second axis λ_2 is not large enough to have $p < 0$. The slope of the linearly growing part is close to unity: assuming to neglect λ_3 as a first approximation, both e and p depend primarily on λ_1 , which is larger for high values of e , but p is lowered a bit by the contribution of the second axis, as can be seen in Equation 2.

This quasi-universality of the $e - p$ relation is useful to estimate the shape properties of the halo population at a certain redshift and to create mock catalogues performing Monte Carlo realisations

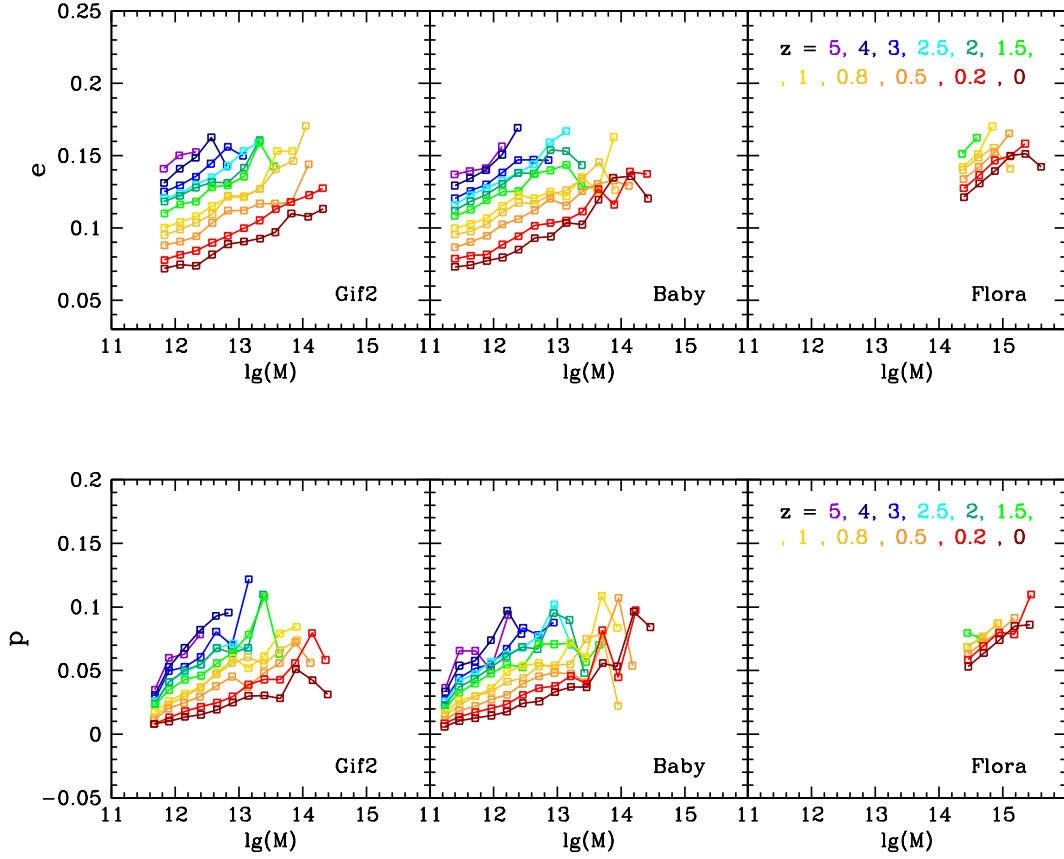


Figure 4. Ellipticity (*top*) and prolateness (*bottom*) median distributions as a function of mass for 13 outputs of both simulations: the three panels refer respectively to the GIF2, Baby and Flora simulations.

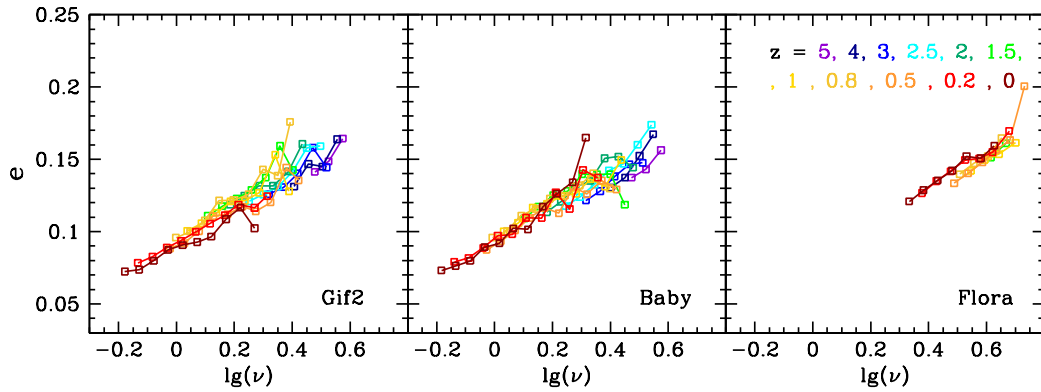


Figure 5. Median Ellipticity as a function of ν : we show the effect of rescaling the mass to the variable ν : since it contains the dependence on epoch and cosmology, all the ellipticity distributions of the previous Figure now lie on the same relation. The color scheme is the same of Figure 4. The rescaling has also the same effect on the prolateness and on the axial ratios.

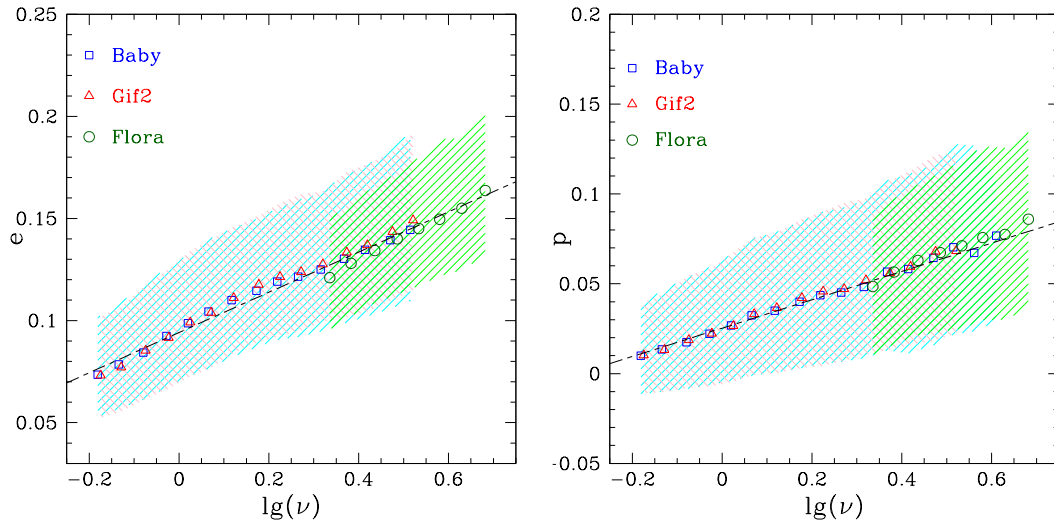


Figure 6. *Universal* ellipticity and prolateness distribution. e and p are shown as a function of the variable $\nu = \delta_c/\sigma$: this choice eliminates the dependence on epoch and, as we see, the distributions at all times lies on same relation. The coloured points show the medians for each simulation and the corresponding shaded coloured regions enclose the first and third quartile of each distribution; the black dashed line represents the best fit to all the points.

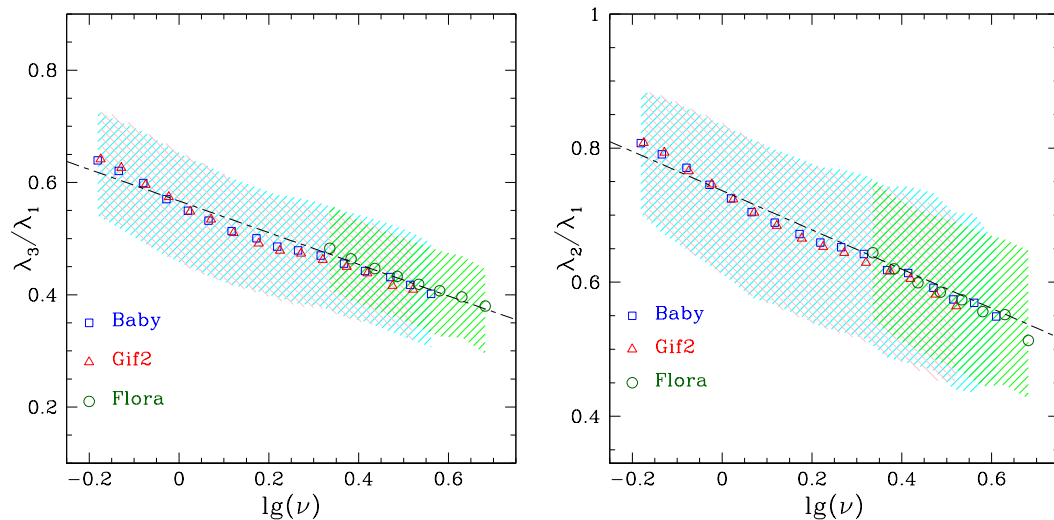


Figure 7. *Universal* axial ratio distributions. The color scheme is the same as in Figure 6

4 MERGER TREE AND FORMATION REDSHIFT

From the halo catalogues, we built the merging history tree for all haloes in the simulations with more than 200 particles: starting from each halo at redshift $z = 0$, we define its progenitors at the previous output $z = z_i$ as all the haloes containing at least one particle of the $z = 0$ halo; we term as "main progenitor" the halo that provided the largest mass contribution to the final one. Then we repeat the same procedure, now starting from the main halo progenitor at the snapshot $z = z_i$ and going backwards in time in this way from snapshot to snapshot, until all the particles are lost in the field (i.e. the main halo progenitor possesses fewer than 10 particles). We stress that our approach to follow the main halo progenitor back in time until it has fewer than 10 par-

ticles is in agreement with previous works and theoretical models developed to interpret the halo mass growth history (van den Bosch 2002; Wechsler et al. 2002; Giocoli et al. 2013). In Figure 9 we show the fit to the formation redshift proposed by Giocoli et al. (2012b) for the Baby and the GIF2 cosmologies, given by the equation:

$$\delta_c(z_f) = \delta_c(z_0) + \bar{w}_f \sqrt{S(fM) - S(M)}, \quad (6)$$

where z_f is obtained by inverting the relation between δ_c and z_f . The parameters are

$$\bar{w}_f = \sqrt{2 \ln(\alpha_f + 1)}, \quad (7)$$

and

$$\alpha_f = \alpha_0 \exp(-2f^3)/f^{0.707} \quad (8)$$

where $\alpha_0 = 0.937$ – corresponding dashed curves for the two cosmologies. The value of α_0 in this case is different from the one computed by Giocoli et al. (2012b) by circa 15% because of the different halo sample considered. While Giocoli et al. (2012b) considered all bounds haloes that never exceed more than 10% their present-day mass along their mass accretion history, in this work we consider all identified systems at the present time. A higher value of α_0 modifies the normalization of the formation redshift-mass relation mainly for large value of f in order to take into account the accretion histories of haloes characterized by major merging events excluded by Giocoli et al. (2012b). In each panel the data points represent the median formation redshift z_f at the time at which the main halo progenitor assembles a fraction f of its present-day mass; the shaded regions of the corresponding colour enclose the first and the third quartiles. From the figure we note that, since the cosmology adopted for Baby (and Flora) has a lower value of σ_8 , its haloes have typically a lower formation redshift. Going from the top left panel to the bottom left one, thus decreasing the value of f , the difference between the two simulations increases up to almost 25% for the redshift at which the main halo progenitor assemble a fraction $f = 0.04$ of its present-day mass.

In Figure 10 we show the relation between the ellipticity of haloes at $z = 0$ and their generalized formation redshifts. The points (squares for Baby and triangles for the GIF2) show the medians of the distribution at a fixed z_f for the four definitions, as in Figure 9, while the coloured shaded regions enclose the first and third quartile. We can see that, using any of the definitions of formation redshifts, final ellipticity and z_f anti-correlate: this is consistent with the behaviour already seen and discussed in Figure 2. It is also interesting to notice that even if Baby and GIF2 simulations have been run with different cosmological parameters, the relation $e - z_f$ is similar once adopted the same formation redshift definition.

5 SUMMARY AND CONCLUSIONS

To characterise how the distribution of halo shapes evolves in time, we analysed a set of three cosmological simulations – GIF2, Baby and Flora, which cover a wide range of halo masses and allow to compare two different cosmologies. We presented the simulations and the post-processing pipeline used to identify the halo population and calculate the shape properties, using the EO halo finder, already described in Despali et al. (2013). Then we discussed the resulting distributions and proposed some best fitting relations.

The main result of this work is the existence of universal distributions of the shape parameters (e , p and the axial ratios), when rescaling the mass to the universal variable $\nu = \delta_c/\sigma$. It allows to eliminate the dependences on cosmology and epoch, moving the distributions of all redshifts all on the same linear relations. Then we report and study other properties of halo shapes, which can be summarised as follows:

- at fixed mass, halo shapes become more elongated at high redshifts; the behavior is qualitative the same for both cosmologies, with a slight difference in the median values due to the difference in formation times of haloes;

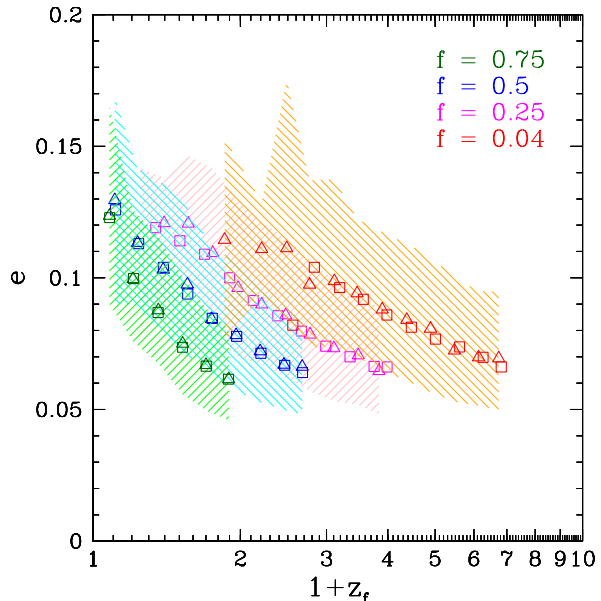


Figure 10. Relation between the ellipticity of haloes at $z = 0$ and the redshift at which haloes assemble different fraction of their mass. The points show the medians of the distribution for all the four definition of z_f , already seen in Figure 9, while the corresponding coloured shaded regions enclose the first and third quartile. The squares show the results for Baby, while the triangles for the GIF2, as in the other figures.

- haloes of similar mass possess larger ellipticity and prolateness at higher redshifts: on average e and p from redshift $z = 2$ to the present time change of about 40 – 50%;
- at any given time, the more massive is an halo, the less spherical it is: this is due to the fact that massive haloes still retain memory of their "original" shape, which has not been yet contaminated or rounded by other events and which is related to the direction of filaments or of the last major merger; thus, at any given time, massive haloes show higher values both of e and p – clearly the same trend is reflected in the axial ratios);
- another quasi-universal distribution is given by the relation between p and e , which remains on average with a slight redshift dependence;
- halo ellipticity is a decreasing function of the generalized formation redshifts z_f – as the redshift when the main halo progenitor assembles a fraction f of its present-day mass, with no particular dependence on cosmology: both GIF2 and Baby cosmology lie on the same relation.

To conclude, halo triaxial properties show a dependence on cosmological parameters since related to the halo assemble histories. In this work we have presented how ellipticity, prolateness and axial ratios correlate with the universal variable ν : in a way that these quantities are independent on halo mass, redshift and background cosmology. We find our results useful to be implemented in a Monte Carlo method to generate mock haloes with given triaxial properties, and in triaxial mass reconstruction methods that require priors for the axial ratio distributions.

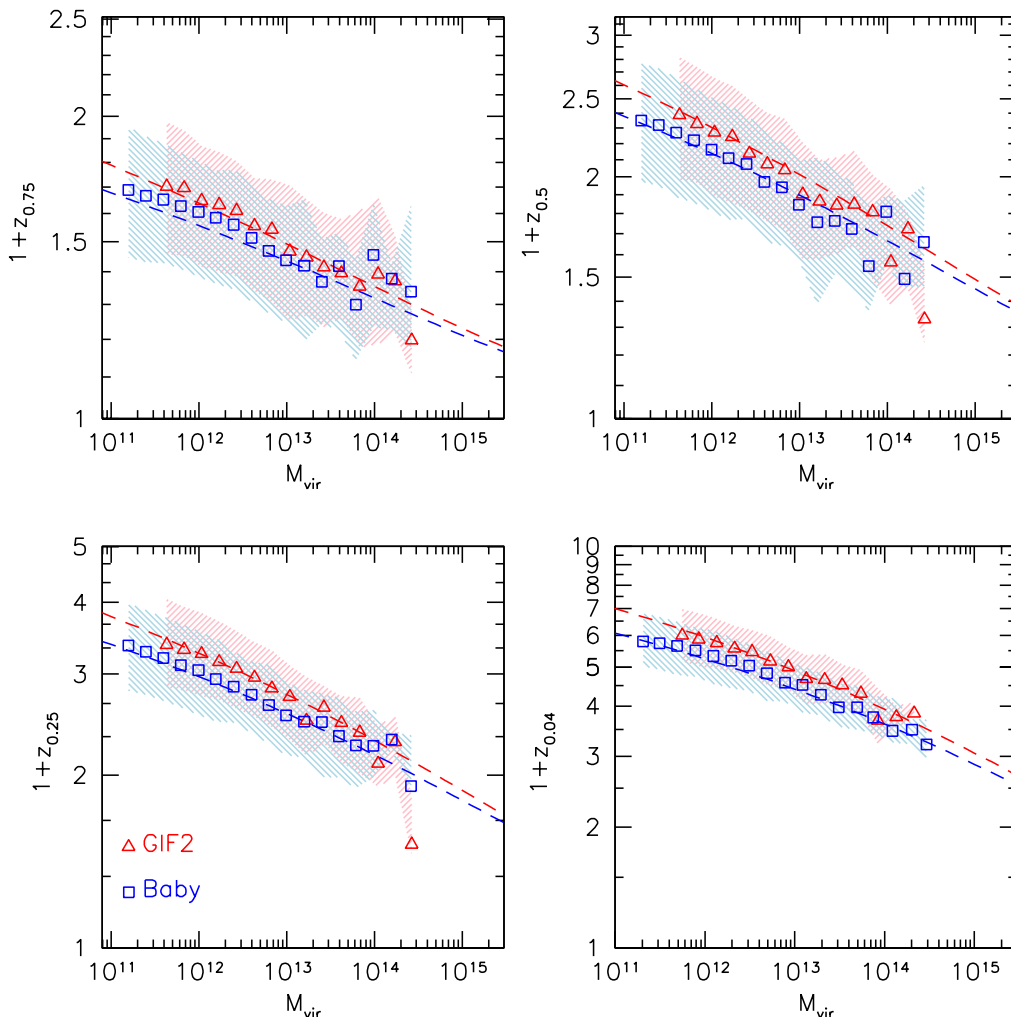


Figure 9. Formation redshift as a function of the halo mass. In the different panels we show the results derived from four definition of formation redshift z_f , defined as the moment at which the main halo progenitor assembles a fraction $f = 0.75, 0.5, 0.25, 0.04$ of its mass. The data points show the median of the measurements performed on the two simulations while the shaded regions enclose the first and third quartiles. The dashed curves represent the predictions for the formation redshift mass relations, for the two cosmologies, using the model by Giocoli et al. (2012b).

6 ACKNOWLEDGEMENTS

We thank Marceau Limousin, Lauro Moscardini and Ravi K. Sheth for reading the manuscript and for their useful comments. We thank Marco Baldi for his help while running the simulations. For this study, GD has been partially financed by the the Strategic Research Project *AACSE* (Algorithms and Architectures for Computational Science and Engineering) of the University of Padova. CG's research is part of the project GLENCO, funded under the European Seventh Framework Programme, Ideas, Grant Agreement n. 259349.

REFERENCES

- Allgood B., Flores R. A., Primack J. R., Kravtsov A. V., Wechsler R. H., Faltenbacher A., Bullock J. S., 2006, *MNRAS*, 367, 1781
- Bardeen J. M., Bond J. R., Kaiser N., Szalay A. S., 1986, *ApJ*, 304, 15
- Becker M. R., Kravtsov A. V., 2011, *ApJ*, 740, 25
- Bond J. R., Cole S., Efstathiou G., Kaiser N., 1991, *ApJ*, 379, 440
- Bond J. R., Myers S. T., 1996, *ApJS*, 103, 1
- Desjacques V., 2008, *MNRAS*, 388, 638
- Despali G., Tormen G., Sheth R. K., 2013, *MNRAS*, 431, 1143
- Eke V. R., Cole S., Frenk C. S., 1996, *MNRAS*, 282, 263
- Ettori S., Morandi A., Tozzi P., Balestra I., Borgani S., Rosati P., Lovisari L., Terenziani F., 2009, *A&A*, 501, 61
- Fu L., Semboloni E., Hoekstra H., Kilbinger M., van Waerbeke L., Tereno I., Mellier Y., Heymans C., Coupon J., Benabed K., Benjamin J., Bertin E., Doré O., Hudson M. J., Ilbert O., Maoli et al. 2008, *A&A*, 479, 9
- Gao L., White S. D. M., Jenkins A., Stoehr F., Springel V., 2004, *MNRAS*, 355, 819

- Giocoli C., Marulli F., Baldi M., Moscardini L., Metcalf R. B., 2013, *MNRAS*, 434, 2982
- Giocoli C., Meneghetti M., Ettori S., Moscardini L., 2012c, *MNRAS*, 426, 1558
- Giocoli C., Meneghetti M., Metcalf R. B., Ettori S., Moscardini L., 2013, ArXiv e-prints
- Giocoli C., Tormen G., Sheth R. K., 2012b, *MNRAS*, 422, 185
- Giocoli C., Tormen G., Sheth R. K., van den Bosch F. C., 2010a, *MNRAS*, 404, 502
- Giocoli C., Tormen G., van den Bosch F. C., 2008, *MNRAS*, 386, 2135
- Jenkins A., Frenk C. S., White S. D. M., Colberg J. M., Cole S., Evrard A. E., Couchman H. M. P., Yoshida N., 2001, *MNRAS*, 321, 372
- Jing Y. P., Suto Y., 2002, *ApJ*, 574, 538
- Lacey C., Cole S., 1993, *MNRAS*, 262, 627
- Lacey C., Cole S., 1994, *MNRAS*, 271, 676
- Lewis A., Challinor A., Lasenby A., 2000, *Astrophys. J.*, 538, 473
- Limousin M., Morandi A., Sereno M., Meneghetti M., Ettori S., Bartelmann M., Verdugo T., 2013, *Space Sci.Rev.*
- Ludlow A. D., Porciani C., 2011, *MNRAS*, 413, 1961
- Marulli F., Baldi M., Moscardini L., 2012, *MNRAS*, 420, 2377
- Marulli F., Bolzonella M., Branchini E., Davidzon I., de la Torre S., Granett B. R., Guzzo L., Iovino et al. 2013, *A&A*, 557, A17
- Meneghetti M., Rasia E., Merten J., Bellagamba F., Ettori S., Mazzotta P., Dolag K., Marri S., 2010b, *A&A*, 514, A93+
- Morandi A., Limousin M., Sayers J., Golwala S. R., Czakon N. G., Pierpaoli E., Jullo E., Richard J., Ameglio S., 2012, *MNRAS*, 425, 2069
- Morandi A., Pedersen K., Limousin M., 2010, *ApJ*, 713, 491
- Morandi A., Pedersen K., Limousin M., 2011, *ApJ*, 729, 37
- Moresco M., Marulli F., Baldi M., Moscardini L., Cimatti A., 2013, ArXiv e-prints
- Muñoz-Cuartas J. C., Macciò A. V., Gottlöber S., Dutton A. A., 2011, *MNRAS*, 411, 584
- Navarro J. F., Frenk C. S., White S. D. M., 1996, *ApJ*, 462, 563
- Neto A. F., Gao L., Bett P., Cole S., Navarro J. F., Frenk C. S., White S. D. M., Springel V., Jenkins A., 2007, *MNRAS*, 381, 1450
- Paranjape A., Sheth R. K., 2012, *MNRAS*, 426, 2789
- Paranjape A., Sheth R. K., Desjacques V., 2013, *MNRAS*, 431, 1503
- Planck Collaboration Ade P. A. R., Aghanim N., Armitage-Caplan C., Arnaud M., Ashdown M., Atrio-Barandela F., Aumont J., Baccigalupi C., Banday A. J., et al. 2013b, ArXiv e-prints
- Planck Collaboration Ade P. A. R., Aghanim N., Armitage-Caplan C., Arnaud M., Ashdown M., Atrio-Barandela F., Aumont J., Baccigalupi C., Banday A. J., et al. 2013a, ArXiv e-prints
- Porciani C., Dekel A., Hoffman Y., 2002, *MNRAS*, 332, 339
- Postman M., Coe D., Benítez N., Bradley L., Broadhurst T., Donahue M., Ford H., Graur O., Graves G., Jouvel S., et al. 2012, *ApJS*, 199, 25
- Prada F., Klypin A. A., Cuesta A. J., Betancort-Rijo J. E., Primack J., 2011, ArXiv e-prints
- Press W. H., Schechter P., 1974, *ApJ*, 187, 425
- Rasia E., Meneghetti M., Martino R., Borgani S., Bonafede A., Dolag K., Ettori S., Fabjan D., Giocoli C., Mazzotta P., Merten J., Radovich M., Tornatore L., 2012, *New Journal of Physics*, 14, 055018
- Roncarelli M., Moscardini L., Borgani S., Dolag K., 2007, *MNRAS*, 378, 1259
- Roncarelli M., Moscardini L., Branchini E., Dolag K., Grossi M., Iannuzzi F., Matarrese S., 2010, *MNRAS*, 402, 923
- Schrabback T., Erben T., Simon P., Miralles J.-M., Schneider P., Heymans C., Eifler T., Fosbury R. A. E., Freudling W., Hettterscheidt M., Hildebrandt H., Pirzkal N., 2007, *A&A*, 468, 823
- Schrabback T., Hartlap J., Joachimi B., Kilbinger M., Simon P., Benabed K., Bradač M., Eifler T., Erben et al. 2010, *A&A*, 516, A63+
- Seljak U., Zaldarriaga M., 1996, *ApJ*, 469, 437
- Sereno M., Ettori S., Umetsu K., Baldi A., 2013, *MNRAS*, 428, 2241
- Sheth R. K., Mo H. J., Tormen G., 2001, *MNRAS*, 323, 1
- Sheth R. K., Tormen G., 1999, *MNRAS*, 308, 119
- Springel V., 2005, *MNRAS*, 364, 1105
- Tinker J., Kravtsov A. V., Klypin A., Abazajian K., Warren M., Yepes G., Gottlöber S., Holz D. E., 2008, *ApJ*, 688, 709
- Tormen G., 1998, *MNRAS*, 297, 648
- Tormen G., Moscardini L., Yoshida N., 2004, *MNRAS*, 350, 1397
- van den Bosch F. C., 2002, *MNRAS*, 331, 98
- Warren M. S., Quinn P. J., Salmon J. K., Zurek W. H., 1992, *ApJ*, 399, 405
- Wechsler R. H., Bullock J. S., Primack J. R., Kravtsov A. V., Dekel A., 2002, *ApJ*, 568, 52
- White S. D. M., 1996, in O. Lahav, E. Terlevich, & R. J. Terlevich ed., *Gravitational dynamics Violent Relaxation in Hierarchical Clustering*. pp 121–+
- White S. D. M., Silk J., 1979, *ApJ*, 231, 1
- Zel'Dovich Y. B., 1970, *A&A*, 5, 84
- Zhao D. H., Jing Y. P., Mo H. J., Bnörner G., 2009, *ApJ*, 707, 354
- Zitrin A., Menanteau F., Hughes J. P., Coe D., Barrientos L. F., Infante L., Mandelbaum R., 2013b, ArXiv e-prints
- Zitrin A., Meneghetti M., Umetsu K., Broadhurst T., Bartelmann M., Bouwens R., Bradley L., Carrasco M. e. a., 2013a, *ApJ*, 762, L30